CHINESE OPTICS LETTERS

Vol. 21, No. 11 | November 2023

Ultrabroadband chiral metasurface for linear polarization conversion and asymmetric transmission based on enhanced interference theory

Jingcheng Zhao (赵京城)[1], Nan Li (李 南)[1,2], and Yongzhi Cheng (程用志)[3,4*]

[1] School of Electronics Information Engineering, Beihang University, Beijing 100191, China

[2] Aerospace Institute of Advanced Material & Processing Technology, Beijing 100074, China

[3] School of Information Science and Engineering, Wuhan University of Science and Technology, Wuhan 430081, China

[4] Hubei Longzhong Laboratory, Xiangyang 441000, China

*Corresponding author: chengyz@wust.edu.cn

Received May 6, 2023 | Accepted July 7, 2023 | Posted Online November 6, 2023

In this paper, we propose an ultrabroadband chiral metasurface (CMS) composed of S-shaped resonator structures situated between two twisted subwavelength gratings and dielectric substrate. This innovative structure enables ultrabroadband and high-efficiency linear polarization (LP) conversion, as well as asymmetric transmission (AT) effect in the microwave region. The enhanced interference effect of the Fabry–Perot-like resonance cavity greatly expands the bandwidth and efficiency of LP conversion and AT effect. Through numerical simulations, it has been revealed that the cross-polarization transmission coefficients for normal forward ($-z$) and backward ($+z$) incidence exceed 0.8 in the frequency range of 4.13 to 17.34 GHz, accompanied by a polarization conversion ratio of over 99%. Furthermore, our microwave experimental results validate the consistency among simulation, theory, and measurement. Additionally, we elucidate the distinct characteristics of ultrabroadband LP conversion and significant AT effect through analysis of polarization azimuth rotation and ellipticity angles, total transmittance, AT coefficient, and electric field distribution. The proposed CMS structure shows excellent polarization conversion properties via AT effect and has potential applications in areas such as radar, remote sensing, and satellite communication.

Keywords: chiral metasurface; linear polarization conversion; asymmetric transmission; Fabry–Perot-like resonance; electromagnetic interference model.

DOI: 10.3788/COL202321.113602

1. Introduction

Metasurfaces (MSs) are planar structures that mimic the behavior of metamaterials (MMs), possessing artificially engineered periodic subwavelength structures. They have garnered significant attention due to their unique electromagnetic (EM) wave-controlling capabilities and low profile characteristics[1]. Chiral metasurfaces (CMSs) represent a notable subset of MSs/MMs, characterized by unit cells that exhibit a geometric structure incapable of being superimposed onto their mirror images through simple translation or rotation. This distinctive geometry induces cross-coupling effects on incident EM waves[2]. CMSs have gained significant attention in recent decades due to their remarkable ability to manipulate EM waves and exhibit exotic properties. These properties include but are not limited to negative refraction[2–4], optical activity and circular dichroism[5–7], polarization-selective absorption[8,9], polarization conversion[10–15], and asymmetric transmission (AT) effect[16–21]. The AT effect, which leads to polarization conversion, is one of the prominent properties exhibited by CMS that has garnered considerable attention. This effect plays a vital role in the design of irreversible EM devices such as radomes, isolators, circulators, and polarization selectors, and holds potential for diverse applications in communication and information systems[22–25]. Polarization conversion refers to the phenomenon where an incident EM wave with a certain polarization is transformed into a different polarization after transmission or reflection through the CMS[10]. Moreover, the AT effect, which is a novel EM phenomenon, was first realized in CMS by Fedotov *et al.* This effect arises from the disparity in the total cross-polarization transmission, resulting in a significant asymmetry

in the proportion of EM waves propagating in the opposite direction of the CMS[16]. Analogous to the unidirectional transmission exhibited by electronic diodes, the AT effect offers an effective approach to selectively block or transmit specific polarization EM waves, independent of the nonreciprocity associated with the Faraday effects[22,23].

In recent years, there has been a growing body of research focused on CMS for achieving the AT effect through various polarization conversion techniques, spanning from the microwave to visible regions of the EM spectrum[18–21,25–37]. For instance, Wang *et al.* proposed a three-layered CMS structure capable of realizing ultrabroad diode-like AT effect for linear polarization (LP) waves and LP conversion effect in the optical region[18]. Cheng *et al.* presented a composite CMS that achieved ultrabroad AT effect for LP conversion with an efficiency exceeding 90% across a frequency range from 4.36 to 14.91 GHz, with a relative bandwidth of about 104.49%[28]. More recently, Habashi *et al.* designed a bilayered CMS that achieved angularly stable LP conversion and AT effect for LP waves at frequencies of 7.5–8.6 and 15–16.6 GHz, respectively[34]. Similarly, Huang *et al.* designed a simple CMS composed of double arc-shaped structures interconnected via two circular cavities, which yielded a broadband AT effect from 4 to 15 GHz for LP conversion[37]. Despite the significant progress in the design and investigation of CMS structures for AT effect through polarization conversion, enhancing the efficiency and operating bandwidth of these structures remains a challenge.

In this study, we introduce a tri-layered CMS design aimed at achieving ultrabroadband and high-efficiency LP conversion and AT effect in the microwave frequency range. The CMS structure is composed of two twisted subwavelength metal gratings and S-shaped resonator (SSR) structures, which are sandwiched with a dielectric substrate, creating a Fabry–Perot-like cavity that enhances the efficiency and operational bandwidth of LP conversion and AT effect. Our proposed CMS design demonstrates the ability to convert the incident LP wave to its orthogonal component of the transmitted LP wave with a polarization conversion ratio (PCR) exceeding 95% across a frequency range from 3.7 to 18 GHz, with a relative bandwidth of 131.79%. The remarkable achievement of giant AT effect within an ultrabroadband frequency range is also demonstrated in this study. The CMS structure is thoroughly analyzed utilizing Fabry–Perot interference theory to elucidate its design and operational mechanism. Comprehensive numerical simulations and experimental measurements are conducted to verify the efficiency of the proposed CMS, revealing excellent agreement among simulation, theory, and experiment. The ultrabroadband and high-efficiency LP conversion and AT effect are further substantiated through PCR, polarization azimuth rotation and ellipticity angles, total transmittance and AT coefficients, as well as the spatial electrical field distribution of the unit-cell structure. These findings highlight the significant potential of the proposed CMS structure for a wide range of microwave applications, including radar, remote sensing, and satellite communication.

2. Structure Design and Fundamental Theory

The CMS design proposed in this study is illustrated in Fig. 1, comprising a metal SSR structure situated between two layers of twisted subwavelength metal gratings, which are separated by a dielectric substrate. The proposed CMS unit-cell, illustrated in Fig. 1(b), comprises three functional layers: the front (I) and back (III) layers, consisting of metal grating structures, and the middle (II) layer, consisting of the SSR structure. The metal grating structures in the front (I) and back (III) layers are designed as typical chiral structures, which can serve as polarization selectors[18,28,38]. This indicates that the grating structure can selectively transmit only a particular polarization (e.g., x-pol.) wave for an arbitrary polarization wave incident normally to the structure, while the orthogonal polarization component (e.g., y-pol.) is significantly blocked. The metal grating structure in the front (I) and back (III) layers is geometrically identical but needs to be twisted at a 90° angle in the x–y plane to produce near-field cross-coupling, which results in a strong chirality. The middle (II) layer of the CMS, which comprises the SSR structure, exhibits its geometric anisotropy and serves as a polarization converter. This means that when a normally incident wave with arbitrary polarization passes through the SSR structure, it can be converted into its orthogonal polarization component upon transmission and reflection[39,40]. The SSR structure exhibits a dipolar resonance in response to a specific electric component of the incident wave, leading to partial LP conversion over a broadband range. The proposed tri-layered CMS forms a Fabry–Perot-like resonance cavity, leveraging the geometric anisotropy and chirality of the structure, which enhances broadband LP conversion via the AT effect. In this design, the Rogers RO4350B (lossy) with relative permittivity of $\varepsilon_r = 3.48(1 + i0.0037)$ is chosen as the dielectric substrate. The copper film pattern with conductivity $\sigma = 5.8 \times 10^7$ S/m is selected as metal layers in the dielectric substrate.

To gain a deeper insight into the operational mechanism of the proposed CMSs, we briefly revisit some fundamental theories pertaining to LP conversion via the AT effect. Considering a plane EM field with E^i propagating in the backward ($+z$)

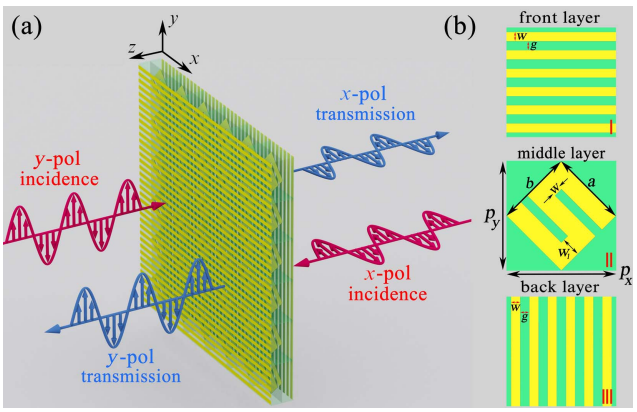

Fig. 1. (a) Schematic diagram of CMS array with the wave propagation, (b) the front (I), middle (II), and back (III) layers of the unit-cell structure.

direction under the Cartesian coordinates of x–y–z, the electric field vectors of the incident, reflected, and transmitted waves along the x-axis and y-axis directions can be mathematically expressed as

$$E^i(r,t) = \begin{pmatrix} E_x^i \\ E_y^i \end{pmatrix} e^{i(kz-\omega t)}, \tag{1a}$$

$$E^t(r,t) = \begin{pmatrix} E_x^t \\ E_y^t \end{pmatrix} e^{i(kz-\omega t)}, \tag{1b}$$

$$E^r(r,t) = \begin{pmatrix} E_x^r \\ E_y^r \end{pmatrix} e^{i(kz-\omega t)}, \tag{1c}$$

where k, ω, E_x and E_y represent the wave vector, angular frequency, and complex amplitudes of electric fields, respectively. The reflection and transmission coefficients are defined as $r_{mn} = E_m^r/E_n^i$ and $t_{mn} = E_m^t/E_n^i$ with the first and the second subscripts m and n (=x, y for LP) denoting the polarization states of the reflected, transmitted, and incident wave, respectively. This indicates that an arbitrary LP wave passing through a CMS structure can be decomposed by two orthogonal components of the transmitted EM waves E_x^t and E_y^t (the complex Jones matrix, T_{li}).

To elucidate the principle of cross-polarization conversion in the tri-layered structure of the proposed CMS, we depict an independent Fabry–Perot-like resonance cavity using an EM interference model in Fig. 2. When the incident wave's electric field (E^i) illuminates the first metal grating layer (I), a special polarization wave (e.g., y-pol., E_y^i) propagates through the I layer and reaches the middle SSR layer (II), while the other polarization wave (e.g., x-pol., E_x^i) is reflected. Similarly, the special polarization wave (e.g., y-pol., E_y^i) reaches the II layer, and a part of it is reflected back to the I layer, while the remaining portion (e.g., y-pol., E_y^i) is converted to another polarization (e.g., x-pol., $E_x^{t'}$) and transmitted to the third metal grating layer (III). The behavior of the III layer is analogous to that of the I and II layers. It is noteworthy that the reflected portion from the III layer is also reflected by the I and II layers, and returns to interact with the III layer again, generating a transmitted electric field. This process continues in an infinite loop. Ultimately, the total transmitted wave is the sum of the waves transmitted from the III layer at each iteration, resulting in an LP conversion (y-pol. to x-pol., E_y^i to E_x^t).

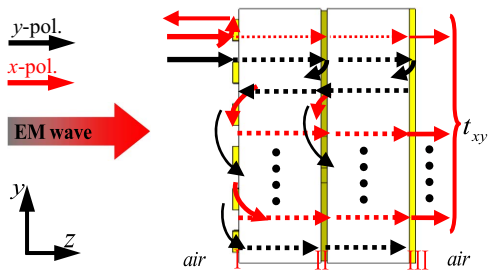

Fig. 2. Enhanced LP conversion mechanism of the Fabry–Perot interference model in tri-layered (I, II, III) structure of the proposed CMS.

The enhanced LP conversion is achieved through the intricate interplay among multiple reflections and transmission interferences taking place among the tri-layered structures of types I, II, and III, as well as the air–substrate interface. The various Fabry–Perot-like scattering processes within the I, II, and III layers can be traced and analyzed. To further investigate the performance of the proposed CMS, the structure is decomposed into I, II, and III layers, and their respective reflection and transmission coefficients are experimentally measured. To establish the relationship between the forward and backward propagating waves at a single interface between two boundary media, denoted as β and α, a 4×4 transfer matrix M_δ can be employed,

$$\begin{pmatrix} \vec{E}_{\beta x} \\ \vec{E}_{\beta y} \\ \overleftarrow{E}_{\beta x} \\ \overleftarrow{E}_{\beta y} \end{pmatrix} = M_\delta \begin{pmatrix} \vec{E}_{\alpha x} \\ \vec{E}_{\alpha y} \\ \overleftarrow{E}_{\alpha x} \\ \overleftarrow{E}_{\alpha y} \end{pmatrix}, \tag{2}$$

and the transfer matrix can be expressed as[41,42]

$$M_\delta = \begin{pmatrix} 1 & 0 & -\overleftarrow{r}_{xx}^{(\delta)} & -\overleftarrow{r}_{xy}^{(\delta)} \\ 0 & 1 & -\overleftarrow{r}_{yx}^{(\delta)} & -\overleftarrow{r}_{yy}^{(\delta)} \\ 0 & 0 & \overleftarrow{t}_{xx}^{(\delta)} & \overleftarrow{t}_{xy}^{(\delta)} \\ 0 & 0 & \overleftarrow{t}_{yx}^{(\delta)} & \overleftarrow{t}_{yy}^{(\delta)} \end{pmatrix}^{-1} \begin{pmatrix} \vec{t}_{xx}^{(\delta)} & \vec{t}_{xy}^{(\delta)} & 0 & 0 \\ \vec{t}_{yx}^{(\delta)} & \vec{t}_{yy}^{(\delta)} & 0 & 0 \\ -\vec{r}_{xx}^{(\delta)} & -\vec{r}_{xy}^{(\delta)} & 1 & 0 \\ -\vec{r}_{yx}^{(\delta)} & -\vec{r}_{yy}^{(\delta)} & 0 & 1 \end{pmatrix}. \tag{3}$$

Here the arrows ($\vec{\bullet}$ and $\overleftarrow{\bullet}$) denote special polarized (e.g., x-pol. and y-pol.) waves propagating in the backward ($-z$) and forward ($+z$) directions, respectively. The subscripts x and y represent the polarization states of the propagating waves in the media denoted as α and β, respectively. The symbols r and t represent the reflection and transmission coefficients of the single interface (denoted as I, II, or III layer), respectively. The superscript δ, which takes values of 1, 2, or 3, corresponds to the respective layer of the metallic structure (I, II, or III). Finally, the four components (t_{xx}, t_{yx}, t_{xy}, t_{yy}) of the transmission matrix can be obtained from the complete M-matrix[43]. Hence, bilayered or tri-layered twisted mutual structures can be employed to construct the CMS. Subsequently, the LP conversion properties of the CMS can be assessed through the aforementioned LP transmission coefficients, which will be discussed in the next section.

3. Simulation and Experiment

To investigate the efficiency and operational mechanism of the designed CMS, comprehensive numerical simulations using the frequency solver in CST Microwave Studio based on the finite-difference time-domain (FDTD) method were conducted for the

unit-cell structure. In the simulations, periodic boundary conditions were implemented in both the x- and y-axis directions (x–y plane) to replicate an infinite array of the CMS, while perfectly matched layers (PMLs) were utilized to simulate the wave propagation direction. Following thorough optimization of the simulation parameters, the final geometric parameters of the CMS unit-cell structure were determined as follows: $p_x = p_y = 9$ mm, $w = g = 0.75$ mm, $w_1 = 1.6$ mm, $t_s = 2.5$ mm.

To further validate the efficiency of the designed CMS, it was fabricated using traditional printed-circuit-board (PCB) technology based on the optimized parameters obtained from the unit-cell structure simulations[44–47]. Figures 3(a) and 3(b) depict portions of the front (I) and middle (II) layers of the final test sample, which has a total area of 180 mm × 180 mm and consists of 20 × 20 unit-cells. Figures 3(c) and 3(d) show the metal grating and SSR structures of the front (I) and middle (II) layers of the unit-cell, respectively. During the fabrication process of the CMS test sample, the metallic patterns of the I and II layers were printed on both sides of the blank RO4350B board, while the III layer was printed on one side of another blank RO4350B board. Subsequently, the II plane and blank plane of the III layer of the two printed boards were carefully glued together. Finally, the total thickness of the designed CMS was approximately 5.1 mm. For measurement purposes, two broadband standard horn antennas were employed, connected to a vector network analyzer (Agilent PNA-X N5244A), to determine the four components (t_{xx}, t_{yx}, t_{xy}, t_{yy}) of the transmission matrix for the incident y-pol. and x-pol. waves propagating along forward ($-z$) and backward ($+z$) directions in an EM anechoic chamber. It is crucial to position the CMS slab at the central location between the two horn antennas during measurements. These antennas were positioned at a significant distance of 2.5 m from each other to mitigate the influence of the near-field effect[28].

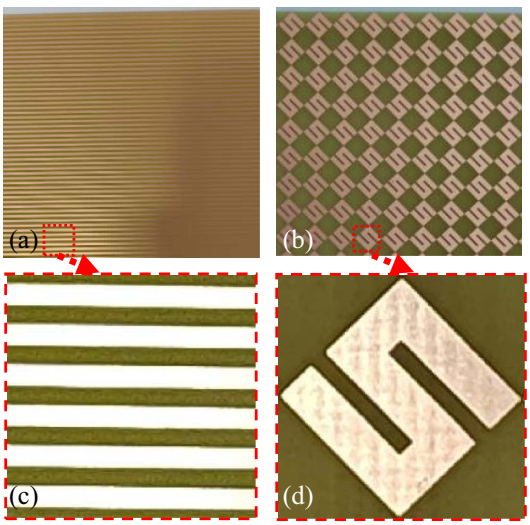

Fig. 3. Fabricated sample of the designed CMS structure. (a), (c) Front layer and (b), (d) middle layer.

4. Results and Discussions

Figure 4 displays the comparison of the LP transmission coefficients (t_{xx}, t_{yx}, t_{xy}, t_{yy}) of the designed CMS as obtained from simulations, calculations, and measurements for the normally incident x-pol. and y-pol. waves propagating along the forward ($-z$) and backward ($+z$) directions. The experimental results exhibit a close agreement with the theoretical calculations and numerical simulations across the desired frequency range. However, there are minor discrepancies observed among the resonance frequencies and magnitudes of the transmission coefficients in the simulation, calculation, and measurement results. Possible explanations for these differences include: (1) slight variations in the permittivity of the RO4350B board substrate and the thickness of the metallic structure during practical fabrication; (2) the consideration of finite sizes of the CMS slab in measurements but not accounted for in the simulation and calculation; and (3) imperfections and tolerances in the test environment.

As depicted in Figs. 4(a), 4(c), 4(d), and 4(f), the results from both simulations and measurements reveal that the cross-polarization transmission coefficients (t_{xy} and t_{yx}) of the CMS for the normally incident y-pol. wave propagating along the forward ($-z$) direction and x-pol. wave propagating along the backward ($+z$) direction exceed 0.8 in an ultrabroadband frequency range spanning 4.13 to 17.34 GHz, with a relative bandwidth of 123.1%. Furthermore, the copolarization transmission coefficients (t_{xx} and t_{yy}) of the CMS for the normally incident y-pol. and x-pol. waves propagating along the forward ($-z$) and backward ($+z$) directions exhibit complete symmetry and remain below 0.1 at the aforementioned ultrabroadband frequencies. This indicates that the designed CMS slab efficiently converts the majority of incident y/x-pol. waves into transmitted x/y-pol. waves, respectively, within an extremely broad frequency range, when planar EM waves propagate along the forward/backward ($-z/+z$) direction. The mechanism behind the ultrabroadband transmission LP conversion is widely attributed to the anisotropic and chiral properties inherent in the unit-cell structure. These properties give rise to intricate transmission

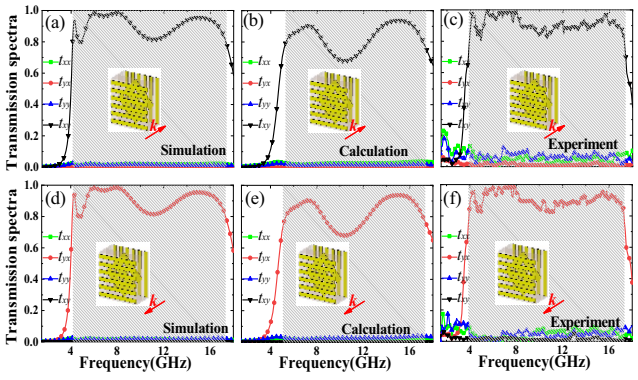

Fig. 4. (a) Simulated, (b) measured, and (c) calculated transmission coefficients (t_{xx}, t_{xy}, t_{yx} and t_{yy}) for the normally incident waves passing through the CMS along (a)–(c) forward ($-z$) direction (d)–(f) backward ($+z$) direction.

and reflection interferences that occur between the tri-layered metallic structures and the interface between air and the Rogers board (see Fig. 2). During the process of LP conversion in transmission, the first metal grating structure in layer I selectively allows for the forward/backward ($-z/+z$) propagation of incident waves polarized along the y/x axis direction. Subsequently, the transmitted y/x-pol. waves undergo conversion to elliptical polarization (EP) with their major axis oriented along the x/y axis direction, facilitated by the SRR structure in layer II. The remaining components of y/x-pol. are reflected and subsequently converted to x/y-pol. waves. In the final step, the metal grating structure in layer III serves to selectively transmit incident y/x-pol. waves, which are almost entirely converted to transmitted x/y-pol. waves, while the residual y/x-pol. waves are primarily reflected. Despite the modest LP conversion efficiency of the SRR structure in layer II, the y/x-pol. waves eventually undergo conversion to the transmitted x/y-pol. waves due to the intricate multiple transmission and reflection processes within the Fabry–Perot-like cavity of the CMS. As a result, the originally unselected LP wave is effectively converted to the desired polarization state via the synergistic interplay of the chirality and anisotropic properties of the Fabry–Perot-like cavity, which induces multiple interference effects. To validate this interpretation, the calculated LP transmission coefficients (t_{xx}, t_{yx}, t_{xy}, t_{yy}) of the designed CMS were obtained using the wave-transfer (4×4 M_{ij}) matrix method, based on the simulated reflection and transmission-matrix elements of each layer, and are shown in Figs. 4(b) and 4(e). These calculated coefficients are found to be in reasonable agreement with both simulation and experimental results. As such, the proposed CMS exhibits an ultrabroadband LP conversion performance for normally incident x-pol. and y-pol. waves propagating along the forward/backward ($-z/+z$) directions, converting y/x-pol. to x/y-pol. respectively.

The LP conversion performance of the designed CMS was validated, as shown in Fig. 5. Simulated, measured, and calculated PCR_x and PCR_y were obtained for x-pol. and y-pol. waves propagating along the forward ($-z$) direction through the CMS. The PCR_y for the normally incident y-pol. wave in the frequency range of 3.7 to 18 GHz is nearly unity, with a relative bandwidth of 131.79%. In contrast, the PCR_x for the incident x-pol. wave remains near zero across the entire frequency range of interest from 2 to 18 GHz. These results indicate that when planar EM waves propagate along the forward ($-z$) direction through the CMS slab [as shown in Fig. 1(a)], only the incident y-pol. wave is selected and completely converted to the transmitted x-pol. wave, while the incident x-pol. wave is reflected by the designed CMS. Conversely, when wave propagation is along the backward ($+z$) direction through the CMS slab, only the incident x-pol. wave is converted to the transmitted y-pol. wave, while the incident y-pol. wave is reflected (not shown).

To demonstrate the LP purity and conversion by 90° polarization rotation, the simulated polarization azimuth rotation angle (θ) and polarization ellipticity angle (η) for normally incident y-pol. wave propagation along the forward ($-z$) direction through the designed CMS are presented in Fig. 6. It can be observed that the value of θ is approximately −90° in the frequency range of 4.23 to 6.13 GHz and 10.78 to 16.39 GHz, while it is approximately +90° in the frequency range of 6.13 to 10.78 GHz and 16.39 to 18 GHz, respectively. This suggests that for normal incidence of y-pol. waves propagating along the forward ($-z$) direction through the designed CMS, there will be complete conversion to the transmitted x-pol. waves through a ±90° LP rotation within the frequency range of 4.23 to 18 GHz. Additionally, the average value of η is close to zero from 3.7 to 18 GHz, indicating that the transmitted wave exhibits exceptional LP purity. This further confirms the ultrabroadband LP conversion capabilities of the proposed CMS.

To showcase the high efficiency of LP conversion via the giant AT effect, we present simulated, calculated, and measured total transmittance (T_x) for x-pol. and y-pol. waves propagating along the forward ($-z$) and backward ($+z$) directions through the CMS. As depicted in Fig. 7(a), when the x-pol. and y-pol. waves with normal incidence are propagating along the forward ($-z$) direction, the simulated total transmittance (T_x) is over 0.5 from 4.12 to 17.71 GHz, whereas it is near zero when the waves are propagating along the backward ($+z$) direction. Furthermore, the peaks of T_x reach up to 0.88, 0.97, and 0.91 at frequencies of 4.32, 7.94, and 14.96 GHz, respectively. This indicates that the designed CMS selectively allows for the transmission of x-pol. waves, while significantly impeding the propagation of y-pol. waves when the incident planar EM wave propagates along the forward ($-z$) direction. As illustrated in

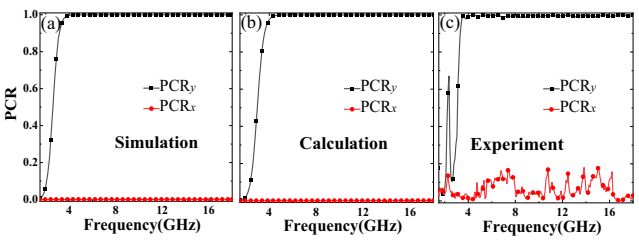

Fig. 5. (a) Simulated, (b) calculated, and (c) measured PCR (PCR_x and PCR_y) for x-pol. and y-pol. waves propagating along the forward ($-z$) direction through the CMS.

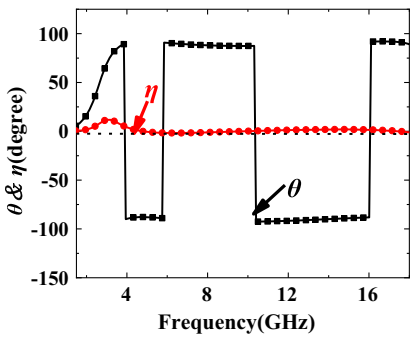

Fig. 6. The simulated polarization azimuth rotation angle (θ) and polarization ellipticity angle (η) were obtained for the normal incidence of y-pol. waves propagating along the forward ($-z$) direction through the designed CMS.

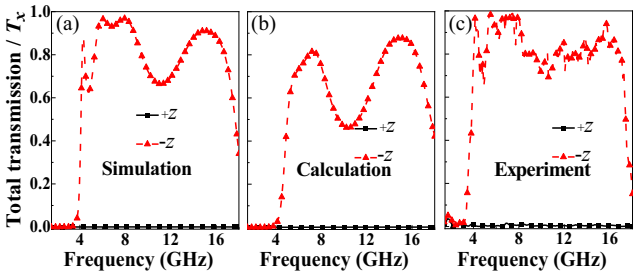

Fig. 7. (a) Simulated, (b) calculated, and (c) measured total transmittance (T_x) for *x*-pol. and *y*-pol. waves propagating along the forward (−*z*) and backward (+*z*) directions through the CMS.

Figs. 7(b) and 7(c), the calculated and measured total transmittances are in reasonable agreement with the simulated results. Evidently, this functionality of the proposed CMS resembles that of a near-perfect ultrabroadband LP wave selector.

Furthermore, to provide further validation of the AT effect exhibited by the designed CMS, the simulated, calculated, and measured AT coefficients (Δ_{lin}) for the normally incident *x*-pol. and *y*-pol. waves are illustrated in Fig. 8. It is evident from the graph that the two curves for Δ_{lin} are completely opposite to each other, and the magnitudes of both curves exceed 0.5 over an ultrabroadband frequency range from 4.12 to 17.71 GHz, with a relative bandwidth of 121.5%. Moreover, the peaks of the AT coefficients are notably high, reaching values of 0.88, 0.97, and 0.91 at typical resonance frequencies of 4.32, 7.94, and 14.96 GHz, respectively. The measured results are in good agreement with the simulations and theoretical calculations in principle. It is worth noting that the AT coefficients for the normally incident circularly polarized wave are close to zero, as indicated in the results (not shown). This confirms that the designed CMS demonstrates a significant AT effect exclusively for LP waves.

It is worth highlighting that the designed CMS has successfully achieved an ultrabroadband AT effect, as confirmed through experimental and theoretical investigations, which is on par with previous studies[19,28,33,36,37]. The proposed CMS design scheme is compared to recently reported designs based on various performance parameters such as bandwidth, efficiency, and AT for broadband LP conversion and AT effect.

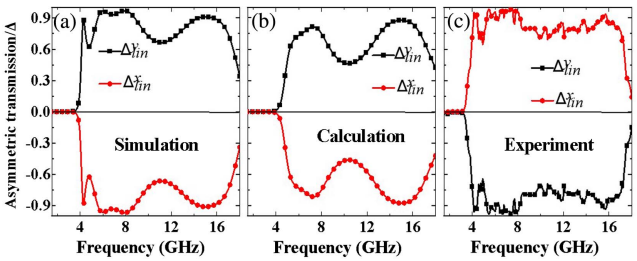

Fig. 8. (a) Simulated, (b) calculated, and (c) measured AT coefficients (Δ_{lin}) for the normally incident *x*-pol. and *y*-pol. waves propagating through the designed CMS.

A clear improvement can be observed from the comparison presented in Table 1.

To provide further insights into the high-efficiency LP conversion via AT effect in the proposed CMS, Fig. 9 showcases the evolution distributions of electric field vectors in the *y*–*z* plane. These distributions encompass the incoming regime, unit-cell structure, and outgoing regime at three representative resonance frequencies: $f_1 = 4.32$ GHz, $f_2 = 7.94$ GHz, $f_3 = 14.96$ GHz, respectively, for normal incidence of *x*-pol. and *y*-pol. waves propagating along the forward (−*z*) direction.

Upon analyzing the electric field vector distributions in Fig. 9, it can be observed that as the normally incident planar EM waves propagate along the forward (−*z*) direction at different resonance frequencies, the *y*-pol. waves undergo complete conversion into transmitted *x*-pol. waves, while the CMS effectively blocks the *x*-pol. waves. Conversely, when the planar EM waves propagate along the backward (+*z*) direction, the situation is reversed, with the *x*-pol. waves being converted to *y*-pol. waves, while the CMS considerably impedes the *y*-pol. waves.

Table 1. Performance Comparison of the Proposed CMS with Previous Works.

References	Frequency Range (GHz)	Bandwidth of PCR (≥ 0.95) (%)	Bandwidth of AT (≥ 0.5) (%)	Thickness (mm)
[19]	8.58–9.73	12.56	11.5	0.786
[28]	4.36–14.91	104.49	103.6	5.1
[33]	9.8–10.5	6.9	5.1	0.8
[36]	19.4–22.7	15.6	11.04	0.8
[37]	6.8–11.9	54.5	53.6	3.0
This work	3.7–18	131.79	121.5	5.1

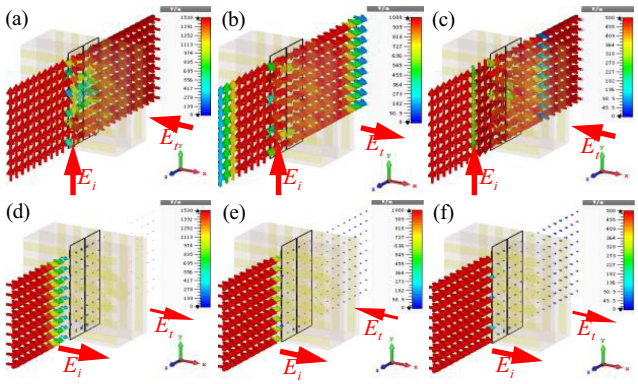

Fig. 9. Simulated electric field vector distributions in the *y*–*z* plane for the CMS unit-cell structure under the normally incident (a)–(c) *y*-pol. and (d)–(f) *x*-pol. waves propagating along the forward (−*z*) direction at different resonance frequencies. (a), (d) f_1 = 4.32 GHz; (b), (e) f_2 = 7.94 GHz; (c), (f) f_3 = 14.96 GHz.

Furthermore, upon closer examination of the electric field vector distributions at lower and higher frequencies of 4.32 and 14.96 GHz, as depicted in Figs. 9(a) and 9(c), it becomes apparent that the polarization of the normally incident y-pol. waves aligns with the $+y$ axis, while the polarization of the transmitted x-pol. waves aligns with the $-x$ axis. Conversely, at the second resonance frequency of 7.94 GHz, the situation is reversed, with the polarization of the transmitted x-pol. waves aligning with the $+x$ axis. This indicates that the incident y-pol. wave will experience a polarization rotation of −90° at frequencies of 4.32 and 14.96 GHz, and a rotation of +90° at 7.94 GHz, which is consistent with the polarization azimuth rotation angle as shown in Fig. 6. It is noteworthy that comparable electric field patterns can also be achieved when planar EM waves propagate in the reverse ($+z$) direction through the proposed CMS (not shown). In such cases, only the x-pol. wave will transform into the transmitted y-pol. wave and undergo a polarization rotation of ±90°. In essence, the field patterns within the unit-cell of the CMS are subject to rotation due to interlayer interference and EM fields coupling effects resulting from the anisotropic and chiral nature of the CMS structure at various resonant frequencies, as reported in previous studies[28,42,48,49]. The observed distributions of electric field vectors within the unit-cell provide further evidence that the CMS has the capability to function as an ultrabroadband 90° LP rotator or converter.

5. Conclusion

In conclusion, this study introduces a novel CMS that features a tri-layered structure comprising an SSR structure array, bilayered twisted metal gratings, and dielectric substrate. This unique structure enables high-efficiency LP conversion and AT effect over an ultrabroadband frequency range. The results obtained from simulations, theoretical calculations, and experimental measurements collectively demonstrate that the proposed CMS is capable of efficiently converting the incident LP wave to its orthogonal counterpart via the AT effect. The experimental results obtained from this study show excellent agreement with the theoretical calculations and numerical simulations. The CMS demonstrates remarkable performance, achieving over 0.8 cross-polarization transmission of the LP wave and over 99% PCR from 3.7 to 18 GHz, with a relative bandwidth of 131.79%. Moreover, the AT parameter exhibits a magnitude of over 0.5 in an ultrabroadband range from 4.12 to 17.71 GHz, with a relative bandwidth of 121.5%. The electric field vector distributions and polarization azimuth rotation angle further confirm the ±90° LP rotation behavior. These findings highlight the potential of the designed CMS for applications in remote sensing, radar, and satellite communication, owing to its ultrabroadband high-efficiency LP conversion via a giant AT effect.

References

1. S. Sun, Q. He, J. Hao, S. Xiao, and L. Zhou, "Electromagnetic metasurfaces: physics and applications," Adv. Opt. Photonics **11**, 380 (2019).
2. Z. Wang, F. Cheng, T. Winsor, and Y. Liu, "Optical chiral metamaterials: a review of the fundamentals, fabrication methods and applications," Nanotechnology **27**, 412001 (2016).
3. J. B. Pendry, "A chiral route to negative refraction," Science **306**, 1353 (2004).
4. Y. Z. Cheng, Y. Nie, and R. Z. Gong, "Giant optical activity and negative refractive index using complementary U-shaped structure assembly," Prog. Electromagn. Res. M **25**, 239 (2012).
5. M. Decker, R. Zhao, C. M. Soukoulis, S. Linden, and M. Wegener, "Twisted split-ring-resonator photonic metamaterial with huge optical activity," Opt. Lett. **35**, 1593 (2010).
6. S. S. Oh and O. Hess, "Chiral metamaterials: enhancement and control of optical activity and circular dichroism," Nano Converg. **2**, 24 (2015).
7. Y. Cheng, Y. Nie, L. Wu, and R. Z. Gong, "Giant circular dichroism and negative refractive index of chiral metamaterial based on split-ring resonators," Prog. Electromagn. Res. **138**, 421 (2013).
8. L. Ouyang, D. Rosenmann, D. A. Czaplewski, J. Gao, and X. Yang, "Broadband infrared circular dichroism in chiral metasurface absorbers," Nanotechnology **31**, 295203 (2020).
9. Y. Cheng, F. Chen, and H. Luo, "Plasmonic chiral metasurface absorber based on bilayer fourfold twisted semicircle nanostructure at optical frequency," Nanoscale Res. Lett. **16**, 12 (2021).
10. Y. Ye and S. He, "90° polarization rotator using a bilayered chiral metamaterial with giant optical activity," Appl. Phys. Lett. **96**, 203501 (2010).
11. Y. Cheng, Y. Nie, Z. Cheng, and R. Z. Gong, "Dual-band circular polarizer and linear polarization transformer based on twisted split-ring structure asymmetric chiral metamaterial," Prog. Electromagn. Res. **145**, 263 (2014).
12. W. Zhu, I. D. Rukhlenko, F. Xiao, and M. Premaratne, "Polarization conversion in U-shaped chiral metamaterial with four-fold symmetry breaking," J. Appl. Phys. **115**, 143101 (2014).
13. Z. Z. Cheng and Y. Z. Cheng, "A multi-functional polarization convertor based on chiral metamaterial for terahertz waves," Opt. Commun. **435**, 178 (2019).
14. J. P. Fan and Y. Z. Cheng, "Broadband high-efficiency cross-polarization conversion and multi-functional wavefront manipulation based on chiral structure metasurface for terahertz wave," J. Phys. D **53**, 025109 (2020).
15. Z. Liu, H. Niu, Y. Lei, B. Zhao, and L. Zhao, "Design of broadband transmission polarization conversion metasurface based on cross–shaped resonators," Appl. Phys. A **128**, 681 (2022).
16. V. A. Fedotov, P. L. Mladyonov, S. L. Prosvirnin, A. V. Rogacheva, Y. Chen, and N. I. Zheludev, "Asymmetric propagation of electromagnetic waves through a planar chiral structure," Phys. Rev. Lett. **97**, 167401 (2006).
17. R. Singh, E. Plum, C. Menzel, C. Rockstuhl, A. K. Azad, R. A. Cheville, F. Lederer, W. Zhang, and N. I. Zheludev, "Terahertz metamaterial with asymmetric transmission," Phys. Rev. B **80**, 153104 (2009).
18. C. Wang, X. Zhou, D. Tang, W. Pan, and J. Dong, "Ultra-broad band diode-like asymmetric transmission of linearly polarized waves based on the three-layered chiral structure," Optik **164** 171 (2018).
19. L. Stephen, N. Yogesh, and V. Subramanian, "Broadband asymmetric transmission of linearly polarized electromagnetic waves based on chiral metamaterial," J. Appl. Phys. **123**, 033103 (2018).
20. B. Han, S. Li, Z. Li, G. Huang, J. Tian, and X. Cao, "Asymmetric transmission for dual-circularly and linearly polarized waves based on a chiral metasurface," Opt. Express **29**, 19643 (2021).
21. Y. Zhang, W. Luan, X. Yan, X. Gao, X. Zeng, Z. Jin, G. Ma, and J. Yao, "Ultra–broadband asymmetric transmission and linear polarization conversion based on terahertz metamaterials," Appl. Phys. B **128**, 156 (2022).
22. R. Singh, E. Plum, C. Menzel, C. Rockstuhl, A. K. Azad, R. A. Cheville, F. Lederer, W. Zhang, and N. I. Zheludev, "Terahertz metamaterial with asymmetric transmission," Phys. Rev. B **80**, 153104 (2009).
23. C. Menzel, C. Rockstuhl, and F. Lederer, "Advanced Jones calculus for the classification of periodic metamaterials," Phys. Rev. A **82**, 053811 (2010).
24. D. L. Sounas and A. Alù, "Non-reciprocal photonics based on time modulation," Nat. Photonics **11**, 774 (2017).
25. D. Yang, Y. Cheng, F. Chen, H. Luo, and L. Wu, "Efficiency tunable broadband terahertz graphene metasurface for circular polarization anomalous reflection and plane focusing effect," Diam. Relat. Mater. **131**, 109605 (2023).
26. D. Liu, Z. Xiao, X. Ma, and Z. Wang, "Asymmetric transmission of linearly and circularly polarized waves in metamaterial due to symmetry-breaking," Appl. Phys. Express **8**, 052001 (2015).

27. X.-J. Shang, X. Zhai, L.-L. Wang, M.-D. He, Q. Li, X. Luo, and H.-G. Duan, "Asymmetric transmission and polarization conversion of linearly polarized waves with bilayer L-shaped metasurfaces," Appl. Phys. Express **10**, 052602 (2017).
28. Y. Cheng, J. Zhao, X. Mao, and R. Gong, "Ultrabroadband diode-like asymmetric transmission and high-efficiency cross-polarization conversion based on composite chiral metamaterial," Prog. Electromagn. Res. **160**, 89 (2017).
29. F. A. Mangi, S. Q. Xiao, Q. A. Arain, I. Memon, and G. F. Kakepoto, "Asymmetric fission transmission of linear-to-circular polarization converter using bi-layer split ring structure," Wirel. Pers. Commun. **99**, 985 (2018).
30. S. Fang, K. Luan, H. F. Ma, W. Lv, Y. Li, Z. Zhu, C. Guan, J. Shi, and T. J. Cui, "Asymmetric transmission of linearly polarized waves in terahertz chiral metamaterials," J. Appl. Phys. **123**, 033103 (2018).
31. W. Liu, W. Wu, L. Huang, Y. Ling, C. Ba, S. Li, Z. Chun, and H. Li, "Dual-band asymmetric optical transmission of both linearly and circularly polarized waves using bilayer coupled complementary chiral metasurface," Opt. Express **27**, 33399 (2019).
32. T. T. Lv, X. Y. Chen, G. H. Dong, M. Liu, D. M. Liu, C. M. Ouyang, Z. Zhu, Y. X. Li, C. Y. Guan, J. G. Han, W. L. Zhang, S. Zhang, and J. H. Shi, "Dual-band dichroic asymmetric transmission of linearly polarized waves in terahertz chiral metamaterial," Nanophotonics **9**, 3235 (2020).
33. M. I. Khan, B. Hu, A. Amanat, N. Ullah, M. J. I. Khan, and A. R. Khalid, "Efficient asymmetric transmission for wide incidence angles using bi-layered chiral metasurface," J. Phys. D **53**, 305004 (2020).
34. A. Habashi, C. Ghobadi, and J. Nourinia, "A dual-broadband h-shaped metasurface for cross-polarization and asymmetric transmission with high stable incidence angle," AEU - Int. J. Electron. Commun. **143**, 154021 (2021).
35. Y. Tian, Z. Chen, F.-F. Ren, Q. Du, and Z. Li, "High-efficiency asymmetric transmission of red-near-infrared light based on chiral metamaterial," Front. Phys. **9**, 676840 (2021).
36. A. Bibi, M. Ismail Khan, B. Hu, S. Iqbal, and I. Khan, "Efficient asymmetric transmission for wide incidence angles using chiral split-ring-resonators," Int. J. RF Microw. Comput.-Aided Eng. **32**, e23224 (2022).
37. X. Huang, H. Gao, J. He, X. Li, X. Li, J. Fan, and L. Guo, "Broadband linear polarizer with high-efficient asymmetric transmission using a chiral metasurface," AEU - Int. J. Electron. Commun. **152**, 154244 (2022).
38. Y. Luo, K. Qiu, Z. Moumni, W. Zhang, J. Zhu, and F. Zhang, "Chiral metasurface design with highly efficient and controllable asymmetric transmission and perfect polarization conversion of linearly polarized electromagnetic waves in the THz range," J. Phys. D **55**, 295303 (2022).
39. N. Li, J. Zhao, P. Tang, and Y. Cheng, "Design of all-metal 3D anisotropic metamaterial for ultrabroadband terahertz reflective linear polarization conversion," Phys. Status Solidi B **260**, 2300104 (2023).
40. J. Zhao, N. Li, and Y. Cheng, "All-dielectric InSb metasurface for broadband and high-efficient thermal tunable terahertz reflective linear-polarization conversion," Opt. Commun. **536**, 129372 (2023).
41. N. K. Grady, J. E. Heyes, D. R. Chowdhury, Y. Zeng, M. T. Reiten, A. K. Azad, A. J. Taylor, D. A. Dalvit, and H. T. Chen, "Terahertz metamaterials for linear polarization conversion and anomalous refraction," Science **340**, 1304 (2013).
42. Y. Cheng, J. Fan, H. Luo, and F. Chen, "Dual-band and high-efficiency circular polarization convertor based on anisotropic metamaterial," IEEE Access **8**, 7615 (2020).
43. C. Menzel, C. Rockstuhl, and F. Lederer, "An advanced Jones calculus for the classification of periodic metamaterials," Phys. Rev. A **82**, 3464 (2010).
44. Y. Z. Cheng, Y. Nie, Z. Z. Cheng, L. Wu, X. Wang, and R. Z. Gong, "Broadband transparent metamaterial linear polarization transformer based on triple-split-ring resonators," J. Electromagn. Waves Appl. **27**, 1850 (2013).
45. J. Wang, J. Zhao, Y. Cheng, H. Luo, and F. Chen, "Dual-band high-gain microstrip antenna with a reflective focusing metasurface for linear and circular polarizations," AEU - Int. J. Electron. Commun. **157**, 154413 (2022).
46. E. Zhou, Y. Cheng, F. Chen, H. Luo, and X. Li, "Low-profile high-gain wideband multi-resonance microstrip-fed slot antenna with anisotropic metasurface," Prog. Electromagn. Res. **175**, 91 (2022).
47. Z. Zhang, Y. Cheng, H. Luo, and F. Chen, "Low-profile wideband circular polarization metasurface antenna with characteristic mode analysis and mode suppression," IEEE Antennas Wirel. Propag. Lett. **22**, 898 (2023).
48. D. R. Yang, Y. Z. Cheng, H. Luo, F. Chen, and L. Wu, "Ultra-thin and ultra-broadband terahertz single-layer metasurface based on double-arrow-shaped resonator structure for full-space wavefront manipulation," Adv. Theor. Simul. **6**, 2300162 (2023).
49. J. Liu, Y. Cheng, F. Chen, H. Luo, and X. Li, "Tri-band terahertz vortex beam generator based on a completely independent geometric phase metasurface," J. Opt. Soc. Am. B **40**, 441 (2023).